A&A 410, 375–388 (2003)
DOI: 10.1051/0004-6361:20031186

Astronomy & Astrophysics

Hot stars mass-loss studied with Spectro-Polarimetric INterferometry (SPIN)

O. Chesneau[1], S. Wolf[2], and A. Domiciano de Souza[3]

[1] Max-Planck-Institut für Astronomie, Königstuhl 17, 69117 Heidelberg, Germany
[2] California Institute of Technology, 1200 E California Blvd., Mail code 105-24, Pasadena, CA 91125, USA
e-mail: `swolf@astro.caltech.edu`
[3] Département d'Astrophysique de l'Université de Nice/Sophia-Antipolis, CNRS UMR 6525, France
e-mail: `Armando.Domiciano@obs-azur.fr`

Received 12 February 2003 / Accepted 18 July 2003

Abstract. We present a prospective work undertaken on Spectro-Polarimetric INterferometry (SPIN). Our theoretical studies suggest that SPIN is a powerful tool for studying the mass loss from early type stars where strong Thomson scattering is present. Based on Monte Carlo simulations, we computed the expected SPIN signal for numerous hot star spectral types covering a broad range of geometries and optical depths. The SPIN technique is based on the detection and comparison of the fringe characteristics (complex visibility) between two perpendicular directions of polarization. The most obvious advantage is its ability to determine the polarization distribution in spherical winds for which no detection of polarization is achievable by classical techniques. In particular, we demonstrate that the SPIN technique is very sensitive to the β parameter from the so-called "β velocity law" for optically thin winds. Moreover, the location where the bulk of polarization is generated can be defined accurately. The required sensitivity for studying main sequence OB star winds is still very demanding (inferior to 0.5%), but the signal expected from denser winds or extended atmospheres is well within the capabilities of existing interferometers. The visibility curves obtained in two perpendicular polarizations for LBVs or WR stars can differ by more than 15%, and their corresponding limb-darkened radii obtained by the fit of these curves by more than 35%. The signal expected from the extended circumstellar environment of Be stars and B[e] appears also to be easy to detect, relaxing the required instrumental accuracy to 1%. For these spectral types, the SPIN technique provide a good tool to extract the highly polarized and spatially confined envelope contribution from the bright star emission.

It must be pointed out that the astrophysical environments investigated here offer a large panel of SPIN observing conditions in terms of geometry and polarization degree. The behavior of the SPIN observables can be transposed, at least qualitatively, to other astronomical objects for which important local polarization is foreseen.

Key words. techniques: interferometric – techniques: polarimetric – stars: early-type – stars: winds, outflows

1. Introduction

Mass-loss is an intrinsic characteristic of hot stars which eject a strong wind during their whole short life. The light from the central star can be strongly polarized by its close circumstellar environment, essentially by Thomson scattering. The mass ejection is mainly driven by the pressure of the intense radiation field mediated by resonant scattering. The young technique of optical interferometry has proven its efficiency to study the close environment of hot stars such as Be star disks (Stee et al. 1995; Quirrenbach et al. 1997; Vakili et al. 1998; Berio et al. 1999) or environment of the Luminous Blue Variable (LBV) P Cyg (Vakili et al. 1997). Without spatial resolution, spectro-polarimetry represents one of the best suited techniques to study any departure from spherical symmetry of the mass-loss (see for instance Taylor et al. 1991 and Wood et al. 1997). The detection of a jet-like structure in the binary β Lyrae with an interferometer (cf. Harmanec et al. 1996) and a spectropolarimeter (cf. Hoffman et al. 1998) illustrates the complementarity of both techniques.

However, the interpretation remains limited by the averaging of the polarized information over the field of view since any observation of nearly symmetrical object provides an almost undetectable signal. For instance, the precision of current photo- and spectro-polarimetric observations is insufficient to test wind models with latitudinal dependance of the mass-loss rate in O supergiants, which predict a continuum polarization of only 0.1 per cent at most (Harries et al. 2002).

Within this context, it appears very attractive to equip a long- baseline interferometer with a polarimetric mode in order to apply the so-called Spectro-Polarimetric INterferometry (SPIN) technique. Such attempts have been performed since the very beginning of interferometry. The unique Narrabri intensity interferometer was used with a polarimeter in

---

Send offprint requests to: O. Chesneau,
e-mail: `chesneau@mpia-hd.mpg.de`

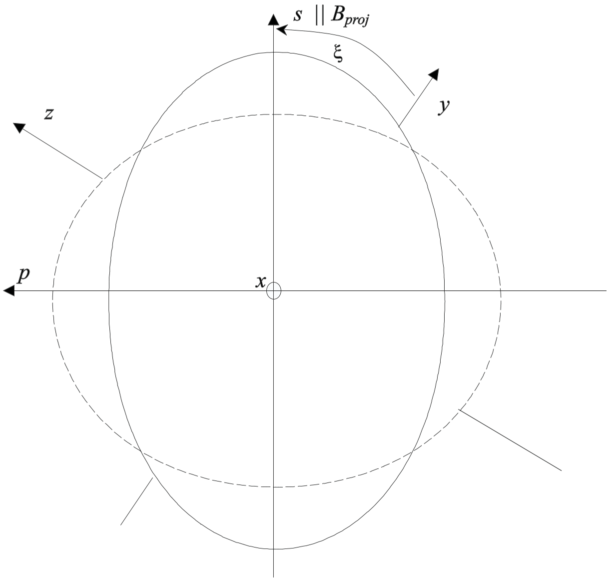

Fig. 1. Adopted reference system. The figure represents isocontours on the apparent disk of a spherical wind as seen with a polarizer parallel (dashed line) and perpendicular (solid one) to the sky projected baseline $\boldsymbol{B}_{\rm proj}$. This axis forms an angle ξ with the sky coordinate system (x, y, z) and defines a new sky projected coordinate system (s, p) for which the s direction is parallel to $\boldsymbol{B}_{\rm proj}$. This (s, p) system is also the frame used in the polarization analysis.

1974 to give an estimate of the polarization-dependent diameter change of β Orionis (Hanbury Brown et al. 1974), but the signal-to-noise ratio (SNR) limitations were well above the expected signal. The experiment was repeated in 1981 with the I2T interferometer on α Lyrae (Vakili et al. 1981), and in 1997 with the GI2T on the Be star γ Cassiopeiae (Rousselet-Perraut et al. 1997). These observations showed that instrumental polarization has to be carefully studied and controlled (Rousselet-Perraut et al. 1997). The first theoretical studies on SPIN were performed in the frame of the Narrabri Interferometer experiment by Sams & Johnston (1974). Cassinelli & Hoffman (1975) investigated the consequences of Thomson scattering around hot stars on the diameter measurements in linearly polarized light (with a single baseline). In the outer regions of the star, the light becomes polarized perpendicular in a direction parallel to the limb of the star. Integrated over the apparent disk this polarization cancels out. In contrast to this, an interferometer in polarization mode can detect a signal due to its sensitivity to the polarized flux in a preferred direction. The star appears smaller in the plane of polarization parallel to the baseline than in the plane perpendicular to it. An illustration of this effect can be seen in Fig. 1, that shows theoretical iso-intensity contours on the disk of the star for two orientations of polarization. Rousselet-Perraut (1998) performed a theoretical study of the SPIN observables based on simple models with spherical and elliptical scattering environments. He also presents a methodology that is useful to interpret the results in the paper.

We intend to present an updated overview of the SPIN capabilities using first, state-of-the-art Monte Carlo simulations, and second a review of the on-going projects in the field of long-baseline optical interferometry (i.e. instrumental facilities, signal performances to be obtained or expected in the near future). We develop a set of astrophysical examples in the field of hot star winds which covers a broad range of wind geometries and intrinsic parameters such as the wind density structure. In Sect. 2, the observables provided by long-baseline optical interferometry are presented, together with the ones more specific for the signal study in polarized light provided by the SPIN technique. Section 3 gives a brief description of the Monte Carlo code MC3D used and adapted for this purpose. In Sect. 4, we deal with spherical winds and perform numerical tests for stars with different spectral types showing significant winds ranging from A supergiants to Wolf-Rayet stars. In Sect. 5, we examine 2D geometries, ranging from anisotropic radiative winds to the disks of Be stars. We then discuss instrumental polarized devices foreseen and needed for such a technique in Sect. 6. Finally, we present the conclusions of this work.

2. SPIN description

In this section we describe the formalism applied in this article. At first, we briefly recall the interferometric observables extracted from natural light. We restrict ourself to the case of a single interferometric baseline, i.e. with two telescopes. We adopt the formalism of Domiciano de Souza et al. (2002) and reproduce here the equations necessary for an introduction to natural light interferometry. In Sect. 2.2 this formalism is then extended to the case of polarized light.

2.1. Natural light

We consider a spherical star defined by its hydrostatic radius $R_{\rm c}$, located at the center of the Cartesian coordinate system *(x, y, z)* shown in Fig. 1. The y axis is defined as the North–South celestial orientation and the x axis points towards the observer.

Let us define the sky-projected monochromatic brightness distribution $I_\lambda(y, z)$, hereafter called “natural light intensity map”. Interferometers measure the complex visibility, which is proportional to the Fourier transform of $I_\lambda(y, z)$. By denoting the Fourier transform of the intensity map by $\widetilde{I}_\lambda(y, z)$ we can write the complex visibility in natural light as:

$$V(f_y, f_z, \lambda) = \left|V(f_y, f_z, \lambda)\right| e^{i\phi(f_y, f_z, \lambda)} = \frac{\widetilde{I}_\lambda(f_y, f_z)}{\widetilde{I}_\lambda(0, 0)}, \tag{1}$$

where f_y and f_z are the Fourier spatial frequencies associated with the coordinates y and z. In long-baseline interferometry the spatial frequencies are given by $\boldsymbol{B}_{\rm proj}\,\lambda_{\rm eff}^{-1}$, where $\lambda_{\rm eff}$ is the effective wavelength of the spectral band considered and $\boldsymbol{B}_{\rm proj}$ is a vector representing the baseline of the interferometer projected onto the sky. The vector $\boldsymbol{B}_{\rm proj}$ defines the s direction, which forms an angle ξ with the y axis so that:

$$\boldsymbol{B}_{\rm proj} = \left(B_{\rm proj}\cos\xi\right)\widehat{y} + \left(B_{\rm proj}\sin\xi\right)\widehat{z}, \tag{2}$$

where $\widehat{y}$ and $\widehat{z}$ are unit vectors.

We consider linear cuts along the Fourier plane corresponding to a given baseline direction $\widehat{s}$. We can define the new spatial frequency coordinates (u, v) for which $\boldsymbol{B}_{\rm proj}$ is parallel to the unit vector $\widehat{u}$. In that case the line integral (or strip intensity) of $I_\lambda(s, p)$ over p for a given ξ can be written as:

$$\widetilde{I}_{\lambda,\xi}(u) = \int I_{\lambda,\xi}(s) \mathrm{e}^{-\mathrm{i}2\pi su} \mathrm{d}s. \tag{3}$$

The *complex visibility* is given by:

$$V_\xi(u, \lambda) = \left|V_\xi(u, \lambda)\right| \mathrm{e}^{\mathrm{i}\phi_\xi(u,\lambda)} = \frac{\widetilde{I}_{\lambda,\xi}(u)}{\widetilde{I}_{\lambda,\xi}(0)}. \tag{4}$$

By varying the spatial frequency (baseline length and/or wavelength), we obtain the so-called visibility curve. Equations (3) and (4) say that the interferometric information along $\boldsymbol{B}_{\rm proj}$ is identical to the one-dimensional Fourier transform of the curve resulting from the integration of the brightness distribution in the direction perpendicular ($\widehat{p}$) to this baseline.

2.2. Polarized light

SPIN allows to derive the geometry of the source as detected with the filtering view of the baseline and the polarization. First, it must be stressed that contrary to classical polarimetry, the polarizer direction is *not* fixed in the celestial North–South direction (y) but related to the baseline direction on the sky (s direction). This is due to the fact that the baseline is fixed to the ground, and not to a moveable mount as in the case of a monolithic telescopes. Thus it appears natural (and it is technically straightforward) that the polarization analysis is using the baseline coordinate system (s, p) showed in Fig. 1. Throughout the entire article, two particular directions for this polarizer are considered: polarizer in s direction (parallel to the baseline) and polarizer in p direction (perpendicular to baseline).

Let $I_{\rm lin}$ represent the polarized light contribution of the intensity map $I_\lambda(y, z)$. Our approach is adapted from the Stokes formalism to our time variable coordinate system of polarization analysis. We simplify the notation by writing $I_{\rm nat} = I_\lambda(y, z)$. We define

$$I_{\rm lin} = I_{\rm parallel} - I_{\rm perpendicular}, \qquad \text{and} \tag{5}$$

$$I_s = I_{\rm nat} - I_{\rm lin} \tag{6}$$

$$I_p = I_{\rm nat} + I_{\rm lin}. \tag{7}$$

When the baseline direction is coincident with the celestial North-South direction, the polarization analysis system is coherent with the Stokes formalism: $I_{\rm lin} = I_{\rm Q}$.

The polarized visibility that is measured by a single baseline is defined by the Fourier transform of the strip intensity of the intensity maps modulated by the polarization (as defined in Sect. 2.1). When we observe with a polarimetric device, we record (simultaneously or not) three quantities: the visibility amplitudes curve $|V|$ in natural light ($|V_{\rm nat}|$) and polarized light ($|V_s|$ and $|V_p|$). These visibilities are related to the corresponding intensity maps I_s and I_p by relations equivalent to Eqs. (3) and (4). These visibilities can then be related to a radius provided that a simple model of the object light distribution is defined (see Sect. 3.3). In order to study the polarized signal, we concentrate in this paper on a few observables chosen for their sensitivity and their simplicity for interpreting the geometry of the source.

We define the polarized deviation curve $\Delta V_P(f)$ as the difference between the visibility curves in polarized light:

$$\Delta V_P(f_y, f_z, \lambda) = |V_p(f_y, f_z, \lambda)| - |V_s(f_y, f_z, \lambda)|. \tag{8}$$

We can also define the degree of polarized visibility (following the formalism from Rousselet-Perraut 1997):

$$P_V(f_y, f_z, \lambda) = \frac{|V_p(f_y, f_z, \lambda)| - |V_s(f_y, f_z, \lambda)|}{|V_{\rm nat}(f_y, f_z, \lambda)|}. \tag{9}$$

The quantities ΔV_P and P_V are obtained at a given time for a given projected baseline. Three regions of the visibility curves are of common interest in stellar interferometry: the first lobe, the first minimum and the second lobe's maximum.

The second lobe's maximum is very sensitive to the limb-darkening law of the star, and is consequently particularly interesting for the study of diffuse light. However, precise observations in these high spatial frequencies require long integration times in order to compensate the low fringe contrast. Moreover, as far as hot stars are concerned, the baselines required for studying the second lobe are generally larger than 200 m in the NIR band, except for the few closest stars. This is also true for the first minimum, commonly used for accurate radius determinations.

Thus, it is more realistic to concentrate on the first lobe. We define the spatial frequency $f_{\rm max}$ as the frequency where the SPIN signal $\Delta V_P(f_{\rm max}) = \Delta V_{\rm max}$ is maximum. The spatial frequency is expressed in units of the inverse stellar radius, $1/R_*$ and in the figures $R_* = R_{\rm c}$. As seen in the following sections, $f_{\rm max}$ occurs at relatively low spatial frequencies, in the $f = (0.2-0.6)\ 1/R_{\rm c}$ range, which relaxes the spatial resolution needed to perform SPIN observations drastically.

3. The Monte Carlo code

3.1. Presentation

The simulation of visibilities and polarimetric observables are based on radiative transfer simulations performed with the Monte Carlo radiative transfer code MC3D (Wolf 2003; see also Wolf et al. 1999; Wolf & Henning 2000). We assume a spherical, extended star which radiates isotropically, i.e., the radiation characteristic at each point of the stellar surface follows the standard cosine law. The radiation field of the star is partitioned into "weighted photons" each of which is characterized by its wavelength and Stokes parameters.

The interaction of the stellar photons with the surrounding electron envelope is described by Thomson scattering. Due to (multiple) scattering events the polarization state of the initially unpolarized photons is modified. In order to derive spatially resolved images of the I, Q, and U Stokes vector components of the configuration, photons leaving the electron envelope are projected onto observing planes oriented perpendicular to the path of the photons. Since the optical depth in the electron envelope in some cases becomes $\ll 1$, the enforced scattering concept introduced by Cashwell & Everett (1959) was applied in order to achieve a high signal-to-noise ratio for the simulated

Table 1. Some relevant parameters for the adopted models of spherical winds. The targets cover the range of spectral type for which strong local polarization are expected. Most of the parameters are adapted from Lamers & Cassinelli (1999), except for α Lyre and for WR 40 with parameters from Aufdenberg et al. (2002) and Herald et al. (2001).

			ζ Puppis	ϵ Ori	Deneb	P Cyg	WR 40
Type			O4If	B0Ia	A2Iae	B1Ia/LBV	WN8
Distance	D	pc	430	410	685	1800	2260
Stellar radius	R_c	$R_\odot$	17	35	172	76	11
Core angular diameter	Θ	mas	0.35	0.8	2.35	0.4	0.04
Stellar temperature	T_*	K	42 000	28 000	8875	19 300	45 000
Mass loss rate	$\dot{M}$	$M_\odot$ yr^{-1}	6×10^{-6}	4×10^{-6}	1×10^{-6}	1.5×10^{-5}	3×10^{-5}
Terminal velocity	v_∞	km s^{-1}	2200	1500	225	210	840
Acceleration coefficient	β		1.0	1.5	3	2.5	1
Optical depth	τ_e		0.2	0.17	0.03	1	3.4

images within a reasonable computing time. This concept has been used in particular in the study of the wind of ζ Puppis presented in Sect. 4.1, and also in Sects. 4.2 and 4.3.

3.2. Limits

In this study, an important limitation is that MC3D determines the polarization due to multiple photon scattering by electrons, but does not include the effects of continuous hydrogen absorption and emission seen in disk-like circumstellar envelopes for example. Consequently, our modelling of a hydrogen disk in Sect. 5 results in an upper limit for the expected interferometric signal from an interferometer, especially for disk studies. This effect is discussed in Sect. 6.

3.3. "Numerical" diameters

For each example treated in this paper, we perform a fit of the numerical visibility curves obtained with the code MC3D in order to derive the apparent diameter Θ_ap, which is by definition larger than the diameter Θ_c defined with the hydrostatic radius R_c. The definition of the parameter Θ_ap is not straightforward but depends on the model used for the fit. If the centre-to-limb variation (CLV) of intensity could be observed directly, an intensity radius could be defined in terms of the CLV shape and then related to a monochromatic optical-depth or filter radius via a model. In practice, reconstruction of the CLV from interferometric data is difficult with presently attainable accuracies and the mean number of visibility points observed for each star. Diameters are usually derived by fitting the visibility of a well-defined artificial CLV like, e.g. a uniform disk (UD), a limb-darkened disc (LD) or a Gaussian intensity distribution to the observed visibility (cf. Jacob & Scholz 2002). The radius estimation based on the Uniform Disk (UD) assumption is not sufficient since we have chosen spectral types for which the diffuse light from Thomson scattering is important. A better way is to perform a fit of the visibilities based on the assumption that the emergent radiation follows a simple cosine limb-darkening law across the disk of the star (Limb-Darkened disk, LD):

$$I = 1 - c_{s/p}(1 - \mu). \tag{10}$$

The two parameters of the fitted function are the LD angular diameter Θ_LD ($\Theta_{\mathrm{LD}s}$ or $\Theta_{\mathrm{LD}p}$ in polarized light) and the limb-darkening coefficient c (c_s or c_p). These LD radii can be related by the canonical UD radius by (adapted from Sams & Johnston 1974):

$$\Theta_{\mathrm{UD}s} = \left(\frac{1 - \frac{7}{15} c_{s/p}}{1 - c/3} \right)^{(1/2)} \Theta_{\mathrm{LD}s}. \tag{11}$$

In order to provide a clear view on the instrumental capabilities offered by contemporary interferometers, we have assumed a theoretical error curve based on a UD visibility curve estimation. Inside the first lobe a good analytical approximation for the visibility uncertainties σV due to the apparent star radius R_ap is given by (Vakili et al. 1997):

$$\frac{\sigma_{R_\mathrm{ap}}}{R_\mathrm{ap}} = \frac{\sigma V}{|2 J_2 (z)|}, \tag{12}$$

where J_2 is the Bessel function of the first kind and second order. In the following, we assume that the interferometer is able to constrain R_ap with a 1% accuracy, and we build the related σV curve. This curve is then overplotted in each ΔV_P diagram (in Figs. 3, 7, 9–11, Fig. 13) as a visual scale of the instrument accuracy for an illustration purpose.

4. Spherical winds

In this section, we consider spherical winds, for which the integrated polarized information averages out to a null value. In Table 1, we present a list of typical early type stars for which the spatial characteristics (i.e. mainly the angular diameter and the brightness) are well suited for interferometric observations. Moreover, their winds are thick enough to expect a clear SPIN signal from their diffuse light. It must be pointed out that the angular diameters reported in this table are not the expected *apparent angular diameters* Θ_ap, but the *core diameter* or Θ_c used as input parameter for the radiative transfer simulation. The expected apparent angular diameter in natural light is increased by the wind as the star appears larger as a result of the diffused light from the halo.

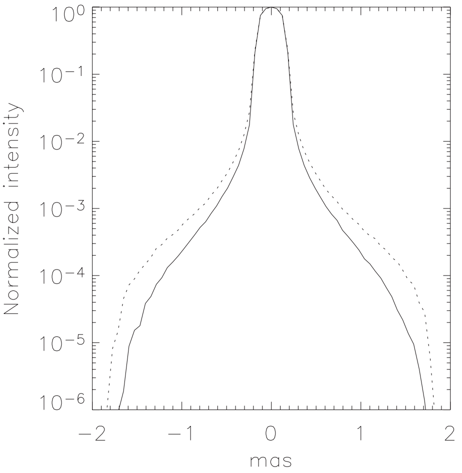

Fig. 2. ζ Puppis flux integrated in the baseline direction (strip intensity map) for polarizations s (solid line) and p (dotted line). Close to the photosphere, the wind density strongly decreases following a rapid acceleration modelled by the β law.

For the wind velocity we apply the so-called β law:

$$v(r) = v_\infty \left(1 - \frac{r_0}{r}\right)^\beta, \tag{13}$$

where

$$r_0 = R_\mathrm{c}\left[1 - \left(\frac{v_0}{v_\infty}\right)^{1/\beta}\right]. \tag{14}$$

The wind velocity is radial, accelerating to the value v_∞. The stellar radius r_0 is defined as the hydrostatic radius R_c and in the following, v_0 is arbitrarily chosen to be 10 km s^{-1}.

The mass loss rate is related to the density and the velocity via the following relation:

$$\dot{M} = 4\pi r^2 \rho(r) v(r). \tag{15}$$

The local density is extracted from this relation for a given β law and mass-loss rate.

4.1. ζ Puppis

In order to illustrate the expected signal from a spherical wind, we modelled the star ζ Puppis (HD 66811), an early O4If supergiant. Davis et al. (1970) have given an estimation of its apparent angular diameter based on a Uniform Disk fit: $\Theta_\mathrm{ap} = 0.42 \pm 0.03$ mas. In the following, we perform a study of the β law parameters and then discuss the ζ Puppis "standard" model.

4.1.1. "Standard" model

The parameters of our "standard model" are described in Table 1. Using this model, we find a maximum visibility deviation $\Delta V_\mathrm{max} = 0.017$ at the spatial frequency $f_\mathrm{max} = 0.47$. Taking $\lambda_\mathrm{eff} = 1\ \mu$m and the angular diameter of ζ Puppis ($\Theta_\mathrm{ap} = 0.42$ mas), this corresponds to a baseline of 300 m, but only 180 m at $\lambda_\mathrm{eff} = 0.6\ \mu$m. As we can see in Fig. 3, such a SPIN signal is close to the detection limit of an interferometer able to detect radius deviations of the order of 1%.

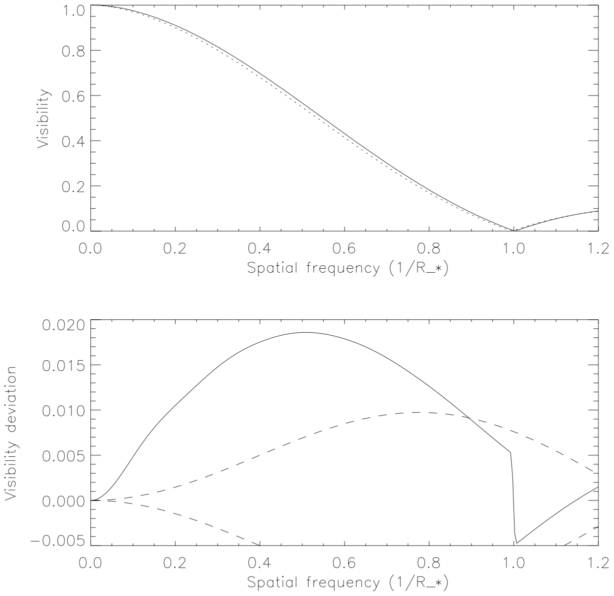

Fig. 3. Visibility signal for both polarization, V_s in solid line, V_p in dotted line (top), and their difference ΔV_P (bottom) for the adopted parameter of ζ Puppis wind. The signal is small, but detectable if the interferometer sensitivity is such that an accuracy of 1% on radii measurements is possible (illustrated by the dashed curves, from Eq. (12)). The discontinuity close to the spatial frequency $f = 1$ appears because the first zero point is located at lower frequency for the polarization p intensity map, slightly more extended than the s one.

Cassinelli & Hoffman (1975) also took ζ Puppis as reference and gave the first estimate of the SPIN signal for a star with a wind. They used a two-component density model for which an extended atmosphere of total thickness $\tau_\mathrm{e} = 10$ is connected to a flow region with an optical thickness $\tau_\mathrm{e} = 0.19$, which is close to our standard parameters. However, their wind follows a different density law:

$$\rho = \rho_0 \left(\frac{R_\mathrm{c}}{r}\right)^n. \tag{16}$$

We have conducted a comparative study with the Cassinelli & Hoffman density law ($n = -2$) and the same τ_e. Compared to our standard ζ Puppis model (with the β law), this new model presents a diffused light multiplied by a factor 2.5. For an equivalent optical depth, ΔV_max is almost doubled, and $f_\mathrm{max} = 0.18$ only, to be compared with $f_\mathrm{max} = 0.47$ in case of our "standard" model. The polarization is generated much farther from the star with the power law model and the optimum baseline to detect the polarized signal taking $\lambda_\mathrm{eff} = 1\ \mu$m (resp. 0.6 μm) should be reduced to 120 m (resp. 70 m).

By performing a least-square fit with a uniform disks to the simulated visibilities, Cassinelli & Hoffman expect an angular diameter ratio between two perpendicular polarization directions of 7%, and Θ_ap from a uniform disk fit of the star emission is 12% larger than the Θ_c. The results from the "standard" model are smaller by a ratio of 2%, and $\Theta_\mathrm{ap} = 1.07\,\Theta_\mathrm{c}$. The contribution from the extended atmosphere included in Cassinelli & Hoffman appears to strongly favor the polarized signal compared to our Monte Carlo simulation of the wind component only. Their result has been confirmed later by Castor et al. (1975) who estimated that the scattering halo of

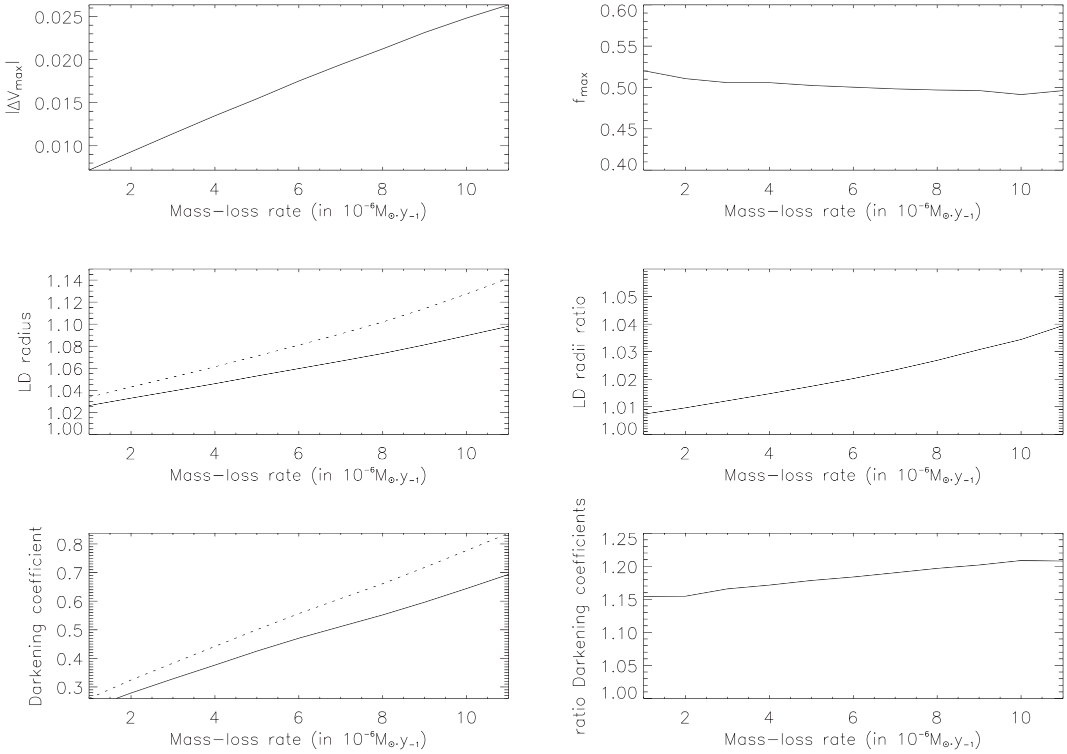

Fig. 4. Top: Behavior of the maximum SPIN signal $\Delta V_{\max}$ and the corresponding spatial frequency $f_{\max}$ with $\dot{M}$. Middle and bottom: result of fits of the polarized visibility curves with a 2 parameters limb-darkening law: LD angular diameters $\Theta_{\rm LDs}$ (solid line) and $\Theta_{\rm LDp}$ (dotted line) and LD coefficients $u_{\rm p}$ (solid line) and $u_{\rm s}$ (lower line). In right the ratio $\Theta_{\rm LDp}/\Theta_{\rm LDs}$ and $u_{\rm p}/u_{\rm s}$ are displayed. As the mass-loss increases, the contrast between $\Theta_{\rm LDp}$ and $\Theta_{\rm LDs}$ increases but $u_{\rm p}/u_{\rm s}$ evolves more slowly.

ζ Puppis increases $\Theta_{\rm c}$ by 13% with a similar mass-loss rate ($\dot{M} = 6.6 \times 10^{-6} M_{\odot}$/yr). Nevertheless a refined study from Kudritzki et al. (1983) showed that the atmosphere of ζ Puppis cannot be considered as extended, which gives a lower limit $\Theta_{\rm c} = 0.38 \pm 0.03$ mas, and a diameter increase of less than 10% in all cases and probably as low as a few percents, close to the result from the present "standard" model.

4.1.2. Mass-loss rate: $\dot{M}$

In this section we investigate how the mass-loss rate may affect the SPIN signal. As expected, we see in Fig. 4 that the SPIN signal $\Delta V_{\max}$ follows the mass-loss rate increase and the subsequent electron density increase almost linearly. The wind from ζ Puppis is optically thin throughout the entire range of mass-loss rate encompassed. The spatial frequency $f_{\max}$ at which this maximum $\Delta V_{\max}$ can be detected is relatively stable. This means that the spatial location where the bulk of the polarization is generated is relatively unaffected by a change of the mass-loss. However, the limb-darkening coefficients $c_{s/p}$, are very sensitive to the increase of diffused light since they are multiplied by a factor larger than 3 as seen in Fig. 4. This means that the relative light distribution, i.e. the balance of diffuse light near and far from the star evolves with the mass-loss. Slight multiple scattering effects are visible for high $\dot{M}$: $\Delta V_{\max}$ evolves more slowly with $\dot{M}$.

4.1.3. Velocity: v_{∞}

Now $\dot{M}$ and β are kept fixed to their "standard" values: $\dot{M} = 6 \times 10^{-6}$ and $\beta = 1$. In Eq. (15), we see that increasing the terminal velocity v_{∞} will decrease the local electron density and the scattering. The influence of a change in this parameter on the local electron density has a similar impact as changing the mass-loss rate. The behavior of the SPIN signal follows the local electron density and the electron optical depth reported in Fig. 5. As mentioned for the mass-loss rate, $f_{\max}$ can be considered as constant. Nevertheless, changing v_{∞} has a greater impact on $\Delta V_{\max}$ than a change of the mass-loss rate: the slope of $\Delta V_{\max}$ versus v_{∞} in Fig. 5 is twice as large as the slope versus $\dot{M}$ in Fig. 4. The differences between the mass loss and velocity plots can be understood by the fact that the optical depth of the wind varies as $\tau_{\rm e} = \dot{M}/v_{\infty}$. Thus, $\tau_{\rm e}$ and the visibility increase proportional to $\dot{M}$ and inversely with v_{∞}. Moreover the modification of v_{∞} in the β law affects the local density close to the star (where the radiative field is strong) significantly by changing the value of r_0. The scattering close to the star is increased by a larger amount by a change of v_{∞} than by a change of $\dot{M}$.

4.1.4. Power-law index: β

This parameter defines the density variation from the star to farther regions. Taking the parameters from the ζ Puppis standard model, we have varied β between 0.8 to 1.5.

We see in Fig. 6, that $f_{\max}$ and $\Delta V_{\max}$ are strongly sensitive to β. This demonstrates that the parameter $f_{\max}$ is very

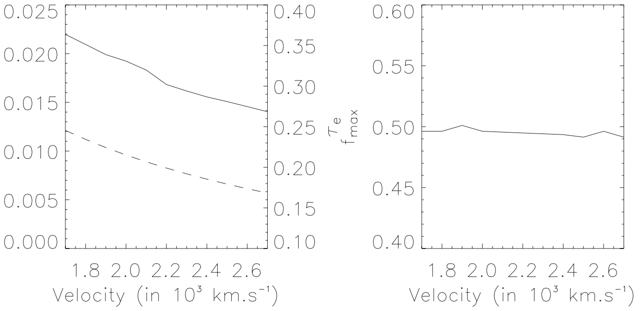

Fig. 5. Behavior of the maximum SPIN signal and the corresponding spatial frequency with parameter v_∞. The dashed curve represents the course of the optical depth τ_e.

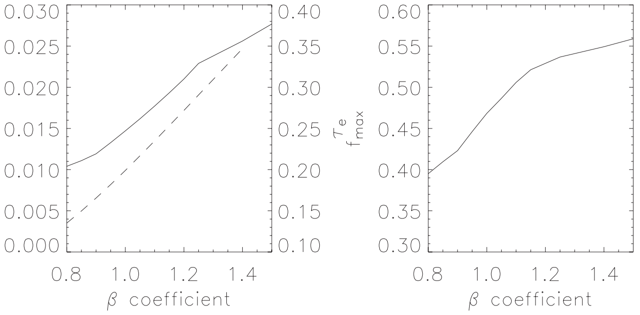

Fig. 6. Behavior of the maximum SPIN signal and the corresponding spatial frequency with parameter β. The dashed curve represents the course of the optical depth τ_e.

sensitive to the main location of the scattered light: *The smaller* $f_{\max}$*, the flatter the density law, i.e. the bulk of the polarized emission is further away from the star*. This behavior is particularly interesting since the β parameter is usually difficult to constrain by classical techniques using spectroscopic data such as spectrum fitting. A change of β has often a small influence on the spectrum itself: the spatial extent of the line forming regions is affected but the lack of spatial information from spectroscopy prevents from constraining efficiently this parameter (see Hillier et al. 1998 for instance). Harries et al. (2002) pointed out recently the sensitivity of the polarized line profile morphology of O supergiants to the adopted velocity field. He suggests that it may be possible to use it as a diagnostic tool for the wind base kinematics. Such a diagnostic could also be performed by an interferometer with sufficient spectral resolution (see discussion in Sect. 6).

4.2. ϵ Ori

The signal expected from ϵ Ori is comparable to the one from ζ Puppis: v_∞ and $\dot{M}$ are similar, and thus τ_e also. But this star is more interesting for interferometric observations since the star is more extended than an O4If star with a similar expected SPIN signal. With $\lambda_{\rm eff} = 0.6$ μm (resp. $\lambda_{\rm eff} = 1$ μm, the baseline of half resolution ($f = 0.5$) is only 70 m (120 m). This means that B supergiants offer a good compromise between polarized signal and spatial resolution. This is especially true for those which exhibit the strongest wind manifestations as LBVs (Sect. 4.4).

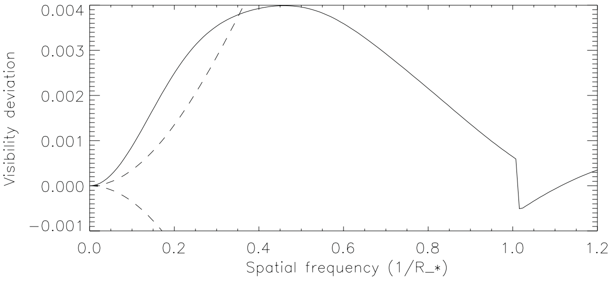

Fig. 7. The expected signal polarization from the Deneb wind model is relatively weak, the ΔV_P curve is below the 1% accuracy illustrated by the dashed curves defined from Eq. (12). Nevertheless, a signal could be still detectable owing to the brightness and the angular diameter of this star.

4.3. Deneb

We performed simulations for Deneb (α Cygni) based on the exhaustive work of Aufdenberg et al. (2002). This A supergiant represents the "cool" detection limit of Thomson scattering in the wind. The β law parameters are estimated from a fit of the numerical electron density law from Aufdenberg et al. (2002) using Eq. (15). The model parameters are displayed in Table 1. The optical depth due to electron scattering is about 7 times lower than for ζ Puppis, and the expected ratio between two perpendicular directions of polarization does not exceed 0.5%. Nevertheless, we expect the results from our Monte Carlo simulation to be a lower limit for the expected SPIN signal produced in the extended atmosphere of this star (Sect. 3.2), and the radius ratio between perpendicular polarizations could be of the order of 1%. The UD angular diameter $\Theta_{\rm ap}$ from Aufdenberg et al. (2002) of 2.4 mas is slightly larger than the core diameter expected from a non-extended atmosphere. However, it must be pointed out that Deneb's Hα profile exhibits a lack of the broad emission wing seen in the spectra of other supergiants, which are normally attributed to electron scattering.

In natural light we expect that the apparent diameter of Deneb remains identical, whatever the baseline direction on the sky may be. The quasi-sphericity of the envelope is well established based on the absence of integrated polarization and detectable variation of radius with baseline for interferometric measurements (Aufdenberg et al. 2002).

4.4. P Cyg

LBVs are instable blue supergiants which cross a short-lived stage of instabilities with large mass loss rate in the HR diagram. The slow, dense wind from LBVs and in particular P Cygni is at least optically thick due to Thomson scattering ($\tau_e = 1$ for P Cygni), and multiple scattering occurs. The observed radius in natural light is very different from the hydrostatic one, defined by the basic P Cygni parameters.

4.4.1. Smooth wind

In Fig. 8 the isocontours of the polarized intensity maps I_s and I_p are shown. They strongly depart from spherical symmetry, and this effect increases with the distance since the local polarization is larger in this case. The diffuse light is important and the angular diameter of the star in natural light represents 135% of the core angular diameter presented in Table 1: $\Theta_{\rm ap} = 0.55$ mas according to the prediction of the detailed P Cygni model of Najarro (2001). The SPIN signal is also large as shown in Fig. 9. The optimum baseline to detect the signal is 110 m (resp. 185 m) with $\lambda_{\rm eff} = 0.6\,\mu$m (resp. 1 μm). But the signal is still strong at shorter baselines: $\Delta V_P = 0.05$ at a normalized spatial frequency $f = 0.15$ (6% visibility difference), which corresponds to a 40 m baseline for $\lambda_{\rm eff} = 0.6\,\mu$m and 70 m for $\lambda_{\rm eff} = 1\,\mu$m. The ratio between radii in perpendicular polarization directions reaches 1.24. The signal amplitude is well within the accuracy of optical interferometers which compensates the fact that the star is not well resolved.

Such a strong SPIN signal is also expected for well-known LBVs such as AG Car, HR Car or HD 316285. The last star has spatial parameters very close to those of P Cygni ones, i.e. an equivalent estimated distance, radius or K magnitude, but differs by its huge mass-loss rate of the order of $2{\times}10^{-4}\,M_{\odot}\,{\rm yr}^{-1}$, more than 10 times larger than that of P Cygni (Hillier et al. 1998). Its wind is very thick ($\tau_{\rm e} \simeq 7$), and the ratio between radii in perpendicular polarized lights reaches 1.37. Due to the high level of multiple scattering, the increase of mass-loss rate does not increase the SPIN signal compared to the case of P Cygni ($\Delta V_{\rm max} = 0.08$). But the bulk of polarized light is generated far from the star and the weight of these extended polarized regions compared to the essentially unpolarized and heavily damped central star increases dramatically. The spatial frequency needed for resolving the polarized halo is consequently much lower compared to the one needed to resolve the central star, and the SPIN signal peaks at $f_{\rm max} = 0.18$. The apparent angular diameter in natural light based on the LD fit reaches $3.0 \times \Theta_{\rm c} = 1.2$ mas (2.5 for the UD angular diameter). It must be noted that the visibility curve of HD 316285 is not adequately described by a Uniform or Limb-Darkened disk visibility fit. For these extreme spectral types fits based on the assumption of a Gaussian distribution of light have to be preferred.

4.4.2. Clumps

The integrated polarization of P Cygni exhibits a strong variability (~0.4%) on time-scales of days to weeks (Taylor et al. 1991), with no favored position angle which implies a quiescent state close to sphericity. This behaviour has been related to strong and localized eruptions and from an in-depth study of the spectopolarimetric variability. Nordsieck et al. (2001) have strongly restricted the "polarized" clump parameter space: position $r < 2R_{\rm c}$, radius $= 0.1R_{\rm c}$, density contrast $\rho/\rho_0 = 20$. These clumps could be related to those detected further out (about 0.5 arcsec) with Adaptive Optics by Chesneau et al. (2000).

Previous interferometric studies have demonstrated that the modulus of the visibility (as used in the paper) is not very sensitive to small scale asymmetries of the object (Vakili et al. 1997). However, the photocenter of the emission in natural and polarized light is no longer centered on the star and consequently affects the phase of the fringes. The expected signal should be faint but a differential study between two polarizations or between line and continuum should increase the accuracy. Such a study for photometry and polarimetry, similar to the one carried out by Rodrigues & Magalhães (2000), is not in the scope of this paper and deserves more extensive investigation.

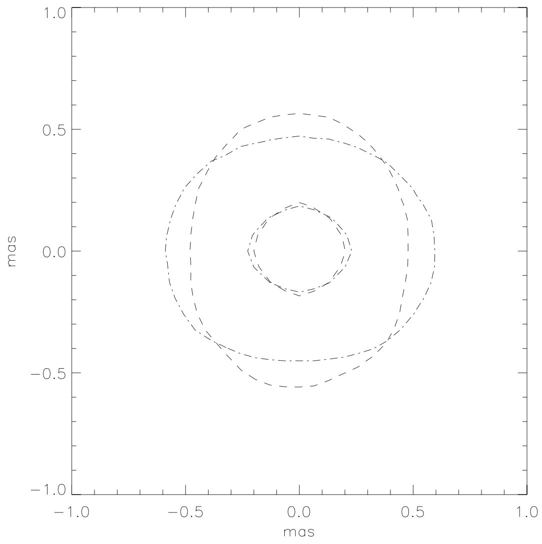

Fig. 8. Square root of polarized intensity maps contours for two perpendicular polarizers for the P Cygni smooth wind model p direction in dashed line and s direction in dashed-dotted line). The inner contour delimits the level $0.8I^2_{\rm max}$, where $I_{\rm max}$ is the maximum of the intensity I. It is close to the core angular diameter of 0.4 mas determined from P Cygni parameters defined in Table 1. The outer contour delimits the level $0.3I^2_{\rm max}$.

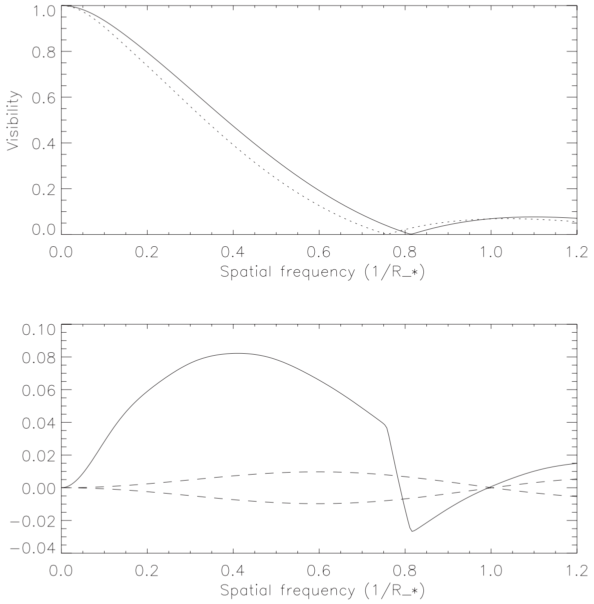

Fig. 9. Visibility V_s (solid line, up) and V_p (dotted line, up) and the SPIN signal ΔV_P (solid line, down) for the P Cygni smooth wind model. The SPIN signal is large and well above the 1% accuracy curves (dashed lines, down). $\Delta V_{\rm max} = 0.087$ at $f_{\rm max} = 0.40$, which corresponds to a relative signal P_V larger than 12%.

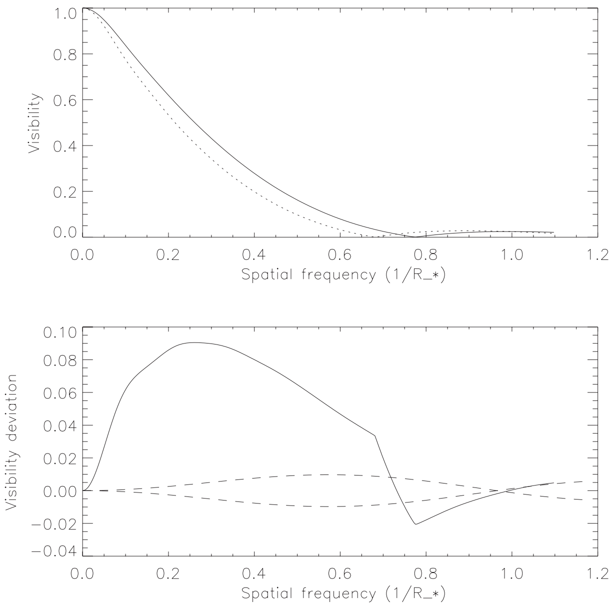

Fig. 10. Visibility V_s (solid line, up) and V_p (dotted line, up) and the SPIN signal $\Delta V_{\rm P}$ (solid line, down) for the WR 40 model. $\Delta V_{\rm P}$ is well above the curves of 1% accuracy (dashed lines, down). The second lobe of the visibility function almost disappears by apodisation for the WR model because the central star is no longer detectable within the envelope.

4.5. WR 40

The Wolf-Rayet (WR) evolutionary stage is characterized by a strong mass-loss rate and a very dense and optically thick wind. These stars also exhibit a much smaller hydrostatic radius, and a faster terminal velocity compared to the LBV stage.

Most of the brightest WR stars are located in distances larger than 1 kpc and their core radii are generally smaller than $4\,R_\odot$ which implies core angular diameters $\Theta_{\rm c}$ lower than 0.04 mas. Nevertheless, the expected apparent diameter can be much larger because the wind is optically thick far from the star. Among WR subtypes, the WN8 star offers a good compromise between luminosity and core radius extent, which reach 10–15 $R_\odot$, and they can therefore be more easily detected with long-baseline interferometers.

The parameters of WR40 are extracted from the dedicated study of Herald et al (2001), and the SPIN signal presented in Fig. 10. As for HD 316285 $\Delta V_{\rm max}$ saturates to the P Cygni value, but the shape of ΔV_P is characteristic of a strongly optically thick wind (see also Cassinelli & Hoffman 1975): $f_{\rm max} = 0.26$, and the visibility curves can no longer be fitted by UD or LD disk visibility laws.

The WR wind parameters are well constrained with current line-blanketed non-LTE models atmospheres. Nevertheless, the constrains on the β parameter are still weak. Herald et al. (2001) investigated β over a range of 0.5–2 and they did not detected any significant impact on their spectra. By varying β, we notice that the SPIN signal is also no longer sensitive to this parameter. The optically thick zone is so large that most of the wind acceleration is embedded in it and the polarization comes essentially from regions close to the terminal velocity. The study of the β law can only be conducted for optically thin winds.

5. Disk geometries

In this section, we investigate objects for which the close environment can no longer be considered as spherically symmetric and presents a 2D structure created by a colatitude dependance of the mass-loss rate. The generated structure can be an extended compressed equatorial region like for B[e] stars or even a disk for Be stars for instance.

5.1. Be stars

Be stars are hot and fast rotating stars surrounded by an extended circumstellar hydrogen envelope. They manifest the so-called "Be Phenomenon" characterized by Balmer lines in emission and infrared excess. One of the challenging questions on Be stars is the geometry of their disk, and in particular their opening angle, about which there is still an active debate. Most authors have considered geometrically thin disks (half opening angle of 2–5°). The very narrow disks considered by Wood et al. (1997) were those predicted by the Wind-Compressed Disks (WCD) theory of Bjorkman & Cassinelli (1993). Furthermore, interferometric observations have given upper limits of approximately 20° (Quirrenbach et al. 1997). However, the hypothesis of such narrow disks faces several problems, and the current set of observations does not provide a unique interpretation on the circumstellar geometry (Yudin et al. 1998).

The model from Waters (1986) has been successfully used to explain the near and far IR observations and is coherent also with polarization data (Coté & Waters 1996; Waters & Marlborough 1992). They model the disk as an equatorial cone with a density law described in Eq. (16) with a density gradient $n \sim 2$–3.5, the density of the disk $\rho_0 \sim 10^{11}$–10^{13} cm^{-3}, the disk radius $R_{\rm d}$, the viewing angle i, and the disk half-aperture θ as main parameters. We performed simulations of the polarized emission of Be star disks. These simulations have been tested using the work from Wood et al. (1996, Fig. 12). We obtain very similar results for the integrated polarization, (with less than 10% deviation) taken into account that our density law is not exactly similar to that used by Wood et al. which allows a colatitude dependency of the density. However, their polar-to-equatorial density ratio of $1 : 10^3$ is very strong, so that we can consider the two models being very close. In particular, we used as template the star ζ Tau (B1 IVe-sh star), which is a well studied case of an edge-on Be star ($i \simeq 82°$; Wood et al. 1997). We used a set of parameters close to those of Wood et al. (1997), i.e., $R_* = 6\,R_\odot$, $T_* = 2 \times 10^5$ K for the central star and a distance of 120 pc. For the disk simulation a very thin disk of half-opening angle of 3° and density law which defines an optical depth in the disk plane of about $\tau_{\rm e} = 3$ (density gradient $n = -3$) are used. We recall that in our study the only emission process considered is Thomson diffusion.

In Fig. 11 we present the expected interferometric signal for ζ Tau for different inclinations. In the pole-on case, we clearly see that the visibility deviation curves $\Delta V_P(f)$ are identical but inverted between both baseline (the baseline is aligned and perpendicular to the polarizer). This configuration is the most favorable for the local polarization: the bulk of electrons

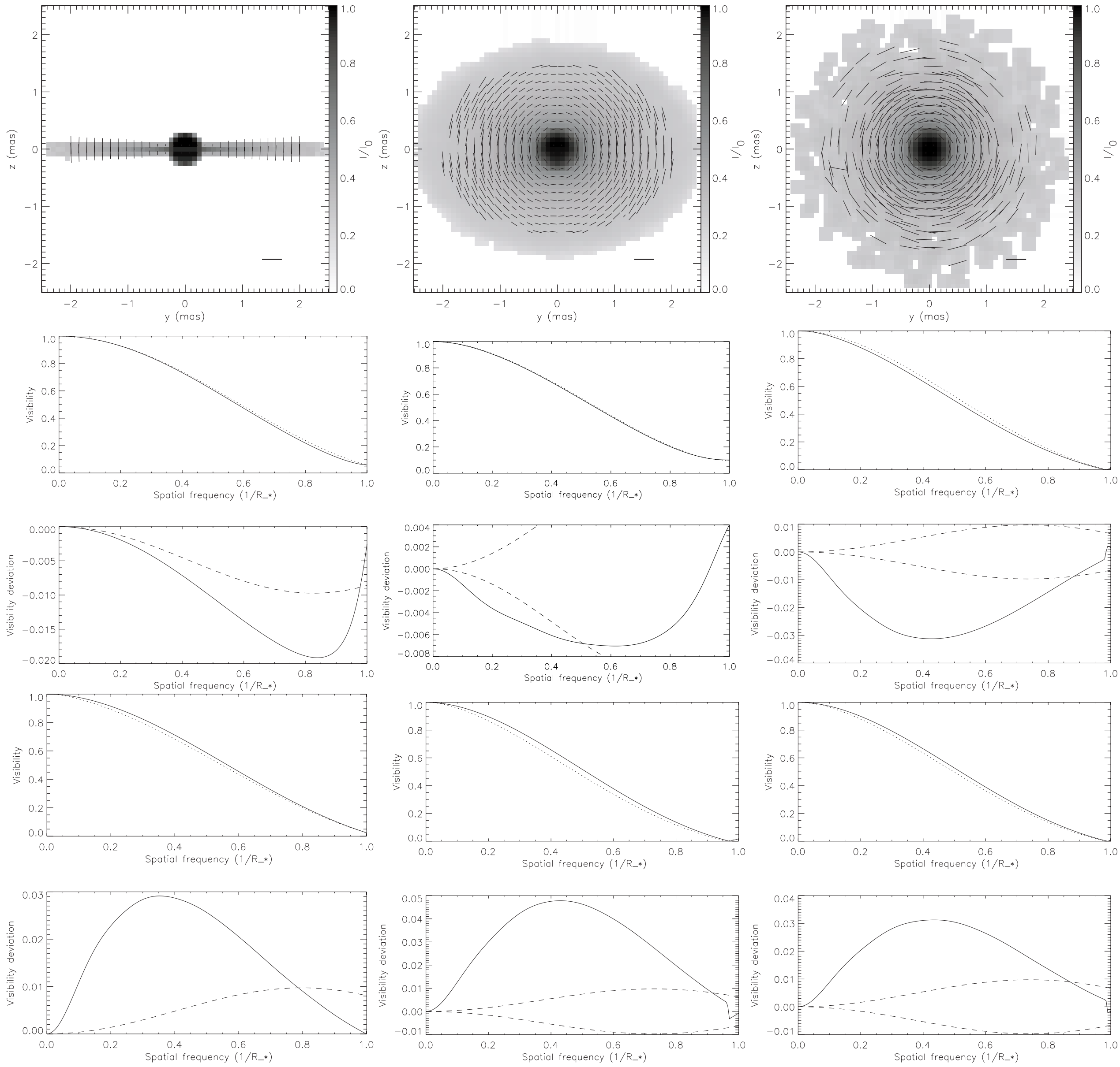

Fig. 11. Model of ζ Tau for 3 inclinations corresponding to 3 disk inclinations (columns). The upper subpanels show the intensity maps on the sky with the overplotted polarization P. The thick bar represents a linear polarization of 100%. The lower panels present the overplotted visibility curves for I_s and I_p maps (s polarization in solid line and p polarization in dotted line), and their difference ΔV_P for a vertical (z, middle panels) and horizontal (y, bottom panels) baseline orientation. For each of the ΔV_P curves corresponds a couple of 1% sensitivity curves (dashed) defined in Eq. (12) to illustrate the strength of the signal.

is perpendicular to the line of sight and $\Delta V_{\max}$ reaches 0.03. For $i = 45°$, the local polarization in the vertical direction is much weaker. This is due to the thinness of the disk: for most of the electrons, the polarization efficiency is only 30% at the diffusion angle $\chi = 45°$ ($P = (1 - \cos(\chi)^2)/(1 + \cos(\chi)^2)$). The SPIN signal is almost undetectable but for the perpendicular baseline, the signal is much stronger ($\Delta V_{\max} = 0.045$). We see in this example that the ratio of ΔV_P between two perpendicular baselines provides valuable information on the system inclination i on the sky and about the aperture of the disk. This complements the natural light information, i.e. the ratio of the radii in two perpendicular directions which provides information on the projected 2D intensity map but no indication on the real 3D structure of the object.

In the equator-on configuration, an unexpected large signal ($|\Delta V_{\max}| = 0.02$) is visible at a high spatial frequency ($f_{\max} = 0.83$) with a vertical baseline (i.e. perpendicular to the disk). This effect is related to the increasing disk vertical extension in the external regions and is strengthened by the absorption of the unpolarized star light in the line of sight. With an horizontal baseline, $f_{\max} = 0.37$, i.e. lower than in the previous case, and $\Delta V_{\max} = 0.03$. This is also due to the optical thickness of the disk, which prevents the observation of high polarization close to the line-of-sight to the star. The bulk of polarization is thus located further out, and $f_{\max}$ is decreased compared to other inclinations.

Figure 12 illustrates the differences and the complementarity between the polarimetric and interferometric observables.

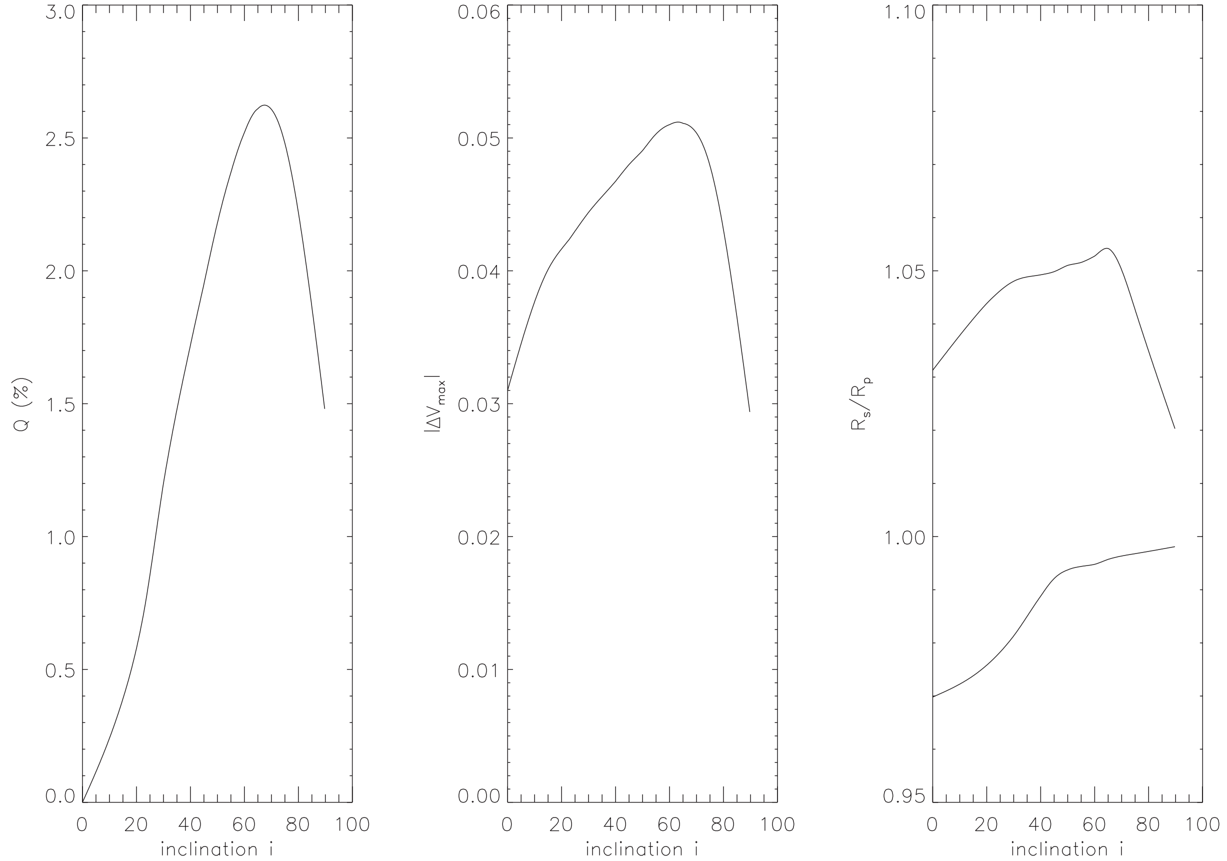

Fig. 12. *Left*: polarimetric and SPIN signal for various inclinations. *Middle*: expected SPIN signal, represented by the maximum of the deviation curve (as shown in Fig. 3). *Right*: Ratio of uniform diameters (UD) fit between two perpendicular polarization direction. The upper (lower) curve describes the ratio $r_{\rm H} = \frac{R_s}{R_p}$ for an horizontal (vertical, $r_{\rm V}$) baseline. Due to the spherical symmetry, the pole-on signal is just inverted between the baseline. At higher inclinations $r_{\rm H}$ increases, but the vertical polarized signal disappears and $r_{\rm V}$ reaches almost 1.

We reproduce quantitatively the integrated polarization curve from Wood et al. (1996). In edge-on view, there is a strong decrease of the local polarization due to the highly optically thick line of sight (multiple scattering). Nevertheless the integrated polarization is compensated by the higher asymmetry of the system (right panel in the figure). In pole-on view the integrated polarization is null but the SPIN signal is still detectable and even slightly larger than in the equator-on case. For integrated polarization and SPIN signals the maximum occurs at the same angle $i \simeq 65°$. The interferometer is very sensitive to the large projected emitting surface of the pole-on view which compensates the lower local polarization.

5.2. B[e] stars

B[e] stars are hot supergiants showing an important excess in the infrared due to the presence of hot circumstellar dust. These stars exhibit also the so-called "Be Phenomenon", but also show forbidden lines in their spectrum. Zickgraf et al. (1985) proposed a model for the LMC B[e] supergiant R126 consisting of a fast wind in the polar regions and a dense and slow wind in the equatorial region where the dust is formed. In contrast to Be stars, the circumstellar geometry of B[e] stars is rather more of an open question. Moreover, within the sample of classified galactic B[e] stars which could be resolved by an interferometer, one can find young stellar objects such as extreme Herbig Be stars (HaebeB[e]), together with supergiant stars (sgB[e], see Lamers et al. 1998). The distance estimations and hence their luminosity and angular diameter are poorly constrained, which render the classification problem. As revealed from their emission lines and near IR (*J* band) excess, the envelopes of sgB[e] stars provide an ample opportunity for scattering of radiation from the central star by free electrons. Moreover, dust is evidenced by their IR excess (Melgarejo et al. 2001). It is possible but sometimes difficult to discriminate the electron scattering and the dust scattering regions with spectropolarimetry alone (Oudmaijer & Drew 1999) and our SPIN technique offers a great help to disentangle between different extents of the polarizing sources. It is not on the scope of this paper to perform a detailed and complex modelling of several examples of sgB[e] stars. We show here the expected impact on the SPIN signal of a typical B[e] stars environment, i.e. an extended, low density scattering region, optically thin and somewhat flattened by using a toy model adapted from Melgarejo et al. (2001).

For that purpose, we use the same model as for the Be stars with a diluted environment (typically $N_{\rm e} \sim 10^9$ cm^{-3}), more open($\theta \sim 5°{-}20°$) and extended (outer radius $R_{\rm outer} \sim 40 R_* - 300\ R_*$), without any dust. The result for an edge-on inclination is shown in Fig. 13. The principal characteristic of this

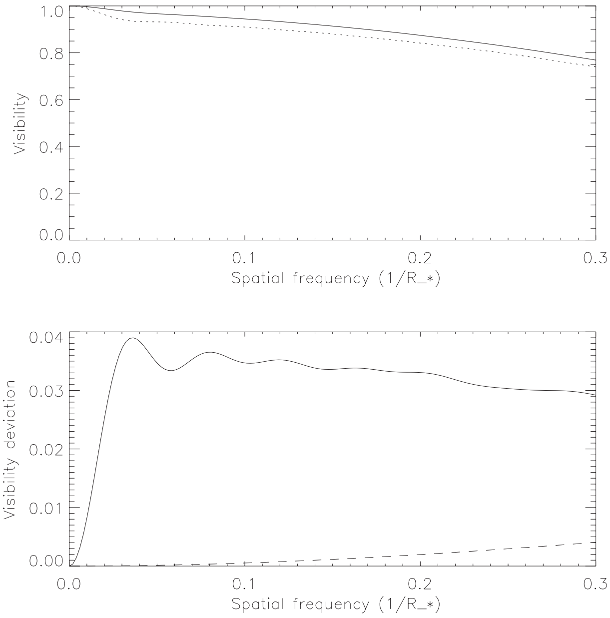

Fig. 13. Model for a B[e] star environment without dust: $N_{\mathrm{e}} = 6 \times 10^9$ cm^{-3} (constant density), $\theta = 10°$, $i = 90°$, $R_* = 70\ R_\odot$, $R_{\mathrm{outer}} = 40\ R_*$, $d = 2$ kpc. $\tau_{\mathrm{e}} = 0.8$ in the disk plane, and the system is seen edge-on. We show a close-up of the two visibility curves $|V_s|$ (solid line) and $|V_p|$ (dotted line). The baseline is aligned to the disk. The contribution of polarized light from the envelope is clearly visible in the oscillation of the polarized differential visibility curve ΔV_P and the signal is well above the 1% sensitivity of a state-of-art interferometer illustrated by the dashed curve. The diffused light represents 8% of the total flux and is almost completely linearly polarized which explains why the envelope signal is concentrated only in one polarization.

environment is the angular diameter contrast between two distinct flux sources: the star and a faint but highly polarized extended envelope. The envelope contribution can be easily seen in Fig. 13. When the baseline and the polarizer are oriented both in the disk direction, the visibility curve is completely dominated by the stellar flux. When the polarizer is aligned with the p direction, the bulk of the envelope becomes visible, superimposed on the stellar component. The envelope is highly resolved so that its contribution is detectable at a low spatial frequency: $\Delta V_{\max} = 0.04$ at $f_{\max} = 0.036$ for the model presented in Fig. 13. The integrated polarization P amounts to 1.8%. The signal amplitude is close to one of the Be star, but its shape is very different due to the contrast between the point-like central source and the very extended and diluted environment.

In conclusion, for B[e], we expect that the SPIN signal from a polarized (by electrons or dust scattering) detached envelope will be easier to extract from the stellar component due to the contrast between star and envelope extents. The envelope polarized and natural relative contribution, its extent and geometry could therefore be retrieved from a relatively simple model of its extracted visibility curve. For Be stars such a simple reduction process is complicated by the fact that the disk extent is much lower, and because the disk is supposed to be highly optically thick for most of the models with small aperture.

6. Instrumental application

After a long development, optical interferometry is now ready to play a significant role in astronomy. The emergence of well-funded interferometer facilities allows to enlarge the field of applications of this technique considerably, by increasing its reliability and its sensitivity. Observing in polarized light with interferometers promises fascinating new insights into many areas of astrophysics, although this capability is difficult to implement with current interferometers. The instrumental polarization in interferometers has been studied by Rousselet-Perraut (1996) and Elias (2001), and we suppose in this section that the SPIN instrument can control and calibrate the effect of the internal polarization on the SPIN observables.

In principle there is no obstacle to equip the focal instrument of an interferometer by polarimetric optics. A simple polarization analyzer using a Wollaston prism can perfectly match the specifications for calibration and visibility determination in the different polarizations. In practice we record fringe patterns in linear polarizations and estimate complex visibilities for each of them. The most promising way to calibrate the signal is to use a differential technique (i.e. by cross-correlating the signal from both polarization directions for instance). The polarized deviation curve can therefore be determined with greater accuracy. It is necessary to use an unresolved star as reference to estimate the absolute visibility. This step can be perfectly carried out only in natural light if the polarized signal can be considered as second-order effect. The first observations have to use large spectral bandwidth to optimize the sensitivity for which a 1% accuracy is expected routinely in natural light.

In the current state-of-the-art of interferometers, it is time consuming to record many visibility points with different baseline lengthes and directions. For spherical targets, the visibility in natural and polarized light does not depend on the projected baseline direction, but only on its length. It means that the data recorded with similar baseline lengths can be added in order to increase the SPIN SNR, since the polarizer direction of analysis follows the baseline movement during observation. For Be and B[e] stars, the measured visibility (in natural or polarized light) does in general not longer depend on the direction of the projected baseline (except for pole-on configurations). The visibility changes with the baseline movement (earth rotation) which restricts the number of visibility points recordable per independent configuration compared to the spherical case. This problem is compensated by the large signal expected from these stars as seen in Sect. 5. It can be somewhat difficult to overcome the degeneracy between disk density, aperture and inclination but the polarized visibility provides an complementary information useful to constrain the parameter space.

Which is the optimum wavelength region for this study? From the polarimetric point of view, the polarized flux generated by Thomson scattering decreases generally in the IR domain due to the competing influence from free-free continuum optical depth τ_{ff}. Since $\kappa_{\mathrm{ff}} \propto a_{\mathrm{ff}}\lambda^2$, the local polarization decreases as $\mathrm{e}^{-a_{\mathrm{ff}}\lambda^2}$. For instance, the integrated polarization of P Cygni is decreased by a factor 3 between 0.55 μm and 1 μm (Nordsieck et al. 2001). It is therefore more interesting to observe towards shorter wavelengths. For Be stars the bound-free

Table 2. Comparison of the SPIN signal between two wavelengths. Be stars radii are estimated from Quirrenbach et al. (1997), and P Cygni radius from this study. The wavelength correction factors are estimated from spectropolarimetric observations: Quirrenbach et al. (1997) for Be stars, and Nordsieck et al. (2001) for P Cygni. In the $f_{\max}$ columns the corresponding baselength are indicated in units of meters. In the ΔV_{50} columns the expected ΔV_P for a 50 m baseline are reported.

Name	Distance	$\Theta_{\rm ap}$	$\lambda_{\rm eff}$ = 0.55 μm			$\lambda_{\rm eff}$=0.66 μm		
	in pc	in mas	$\Delta V_{\max}$	$f_{\max}$	ΔV_{50}	$\Delta V_{\max}$	$f_{\max}$	ΔV_{50}
γ Cas	190	0.56	0.05–0.06	100	≃0.02	0.03–0.04	120	≃0.015
ζ Tau	130	0.4	0.02–0.03	130	≃0.015	0.015–0.025	160	<0.01
η Tau	110	0.71	0.03–0.04	40	≃0.035	0.025–0.03	50	≃0.025
P Cygni	1800	0.55	0.08–0.09	100	≃0.05	0.065–0.075	120	≃0.04

opacities cannot be neglected. In Table 2, we present semi-quantitative signal expectations for Be stars and P Cygni computed by means of the spectro-polarimetric data available for these stars. As an example, the spatially integrated polarization of γ Cas declines from 0.6% at the Balmer jump, to reach 0.52% at 0.5 μm, and 0.4% at 0.66 μm. This evolution reflects only the changes in the free-bound opacity and free-free emission towards the envelope and affects the local polarization and the SPIN signal. The differences between the spectrophotometry of η Tau (nearly pole-one), γ Cas ($i \simeq 45°$) and ζ Tau (nearly edge-on) are mainly due to inclination effects.

The IR domain is also less attractive in term of spatial resolution. This is particularly striking in the context of hot stars since even for the examples presented in this paper, the minimum baseline range needed to resolve the polarized environment is 150–200 m, i.e. at the upper limit of possible VLTI baselines. The number of available baselines for such a scientific task is thus dramatically decreased.

On the other hand, the disturbing effect from the atmosphere is more striking in the optical, and the interferometers able to perform observations in the optical wavelength range are currently few, and somewhat less sensitive than NIR ones. We nevertheless estimate that the gain in spatial resolution and polarized signal is such that the visible wavelength range should be preferred for SPIN observations of hot stars environments, at least for electron scattering studies. We also want to mention the numerous applications of SPIN for the study of dusty environments studies, which are not directly in the scope of this paper. For these environments, the requirements in terms of spatial resolution are strongly decreased, and the IR domain is best suited.

At that moment, only one long-baseline interferometer, the GI2T, is equipped with a polarimeter device for routine observations. The GI2T-REGAIN spectro-interferometer is composed of two 1.5-m telescopes which can be displaced on a North-South baseline spanning from 12 m to 65 m. The REGAIN beam combiner forms the focus in visible light and is equipped with a visible spectrograph in whch a polarimetric device can be inserted. For a complete optical scheme and the status of the instrument, see Mourard et al. (2000a, 2002). The technical description of the polarimetric observation can be found in Rousselet-Perraut et al. (2002).

In the near future, further instruments will provide polarimetric facilities. For instance, the foreseen near-infrared AMBER/VLTI could observe, in a first phase, with a polarimetric device which processes only half of the incoming light. This device has been implemented in order to control the instrumental polarization, but this technical constrain could become a great opportunity to test the SPIN technique since it allows to extract directly the ΔV_P parameter.

A concept of a polarimetric interferometer for the Very Large Telescope Interferometer (VLTI), VISPER (VLTI Imaging Spectro-PolarimetER) has been presented by Vakili et al. (2001). Since great care was taken on instrumental polarization effects during the design and construction of the VLTI, polarimetry could be straightforwardly implemented in the interferometric laboratory. The large baselines, high-order adaptive optics (in the optical), fringe tracking and the foreseen dual-field facility PRIMA can greatly enhance the sensitivity of an interfero-polarimeter to the measurement of small polarization effects on the visibility and extend the number of stars for which a SPIN signal can be detected. Finally, the SPIN technique implies that the observations are carried out with a certain spectral resolving power. This resolving power could allow a study of the visibility through stellar spectral lines in a similar way as spectropolarimetry. The differential information provided by a comparison between the continuum and the lines is richer and more sensitive than the one provided by classical interferometric technics. It allows to retrieve the differential phase information, related to the evolution of the stellar photocenter through the spectrum, and also a dynamic information on the polarized environment through a spectral line (see Vakili et al. 1997; Berio et al. 1999). With PRIMA the calibration can be even carried out in an absolute way. As an example, the hot star emission lines can often be considered as unpolarized and offer a good opportunity to differentially calibrate the polarized continuum, especially for WR stars. The dynamically complex environment of Be stars could also be studied with SPIN. Poeckert & Marlborough (1978) have demonstrated that the Hα line is polarized and contains information on the disk structure and dynamics. This subject should be investigated in a future work.

7. Conclusions

Spectro-Polarimetric INterferometry is a new and complementary way to study the polarized light from hot star environments. The purpose of this article is to present an overview of the potential of the SPIN technique, limited to the study of Thomson scattering within the wind of hot stars. The main point of the SPIN concept is that the star appears to have a different radius depending on the orientation of the polarizers relative to the baseline. This investigation demonstrates that state-of-the-art optical interferometers can detect the visibility difference (the "SPIN signal") for a broad range of stellar wind parameters. The signal is particularly large for the denser winds and can be detected with small baselines (50–150 m). For stars exhibiting dense winds, the envelope is extended and polarized by a large amount whereas the direct, mostly unpolarized stellar light is damped by the scattering, and only barely resolved by the interferometer. The SPIN technique also provides a great wealth of information on Be star disks: disk radii in natural light for different baselines, the difference of visibilities between two direction of polarization *and* baseline orientations. When the spatial scales of the polarized environment and the central star are different, the extraction of the spatial information is simplified, as seen for B[e] stars.

This work has also to be seen in a larger context. The signal modelled in this study is certainly not the largest expected from non-extended astrophysical targets. The environments described here are geometrically and physically similar to astronomical objects ranging from the dusty environment of Young Stellar Objects, AGB stars to the complex environment of AGNs whose apparent angular diameter is equivalent to the targets presented here. Thus, we strongly advocate the development of interferometric devices dedicated to SPIN measurements within the frame of second generation VLTI instruments.

Acknowledgements. The authors thank J. P. Aufdenberg for having provided a numerical detailed model of Deneb. O.C. is grateful to the "Max-Planck Institut für Astronomie" for a postdoctoral grant. S.W. acknowledges financial supported through the NASA grant NAG5-11645, through the grant DP.10633 (project 101555) and through the SIRTF Legacy Science program through an award issued by JPL/CIT under NASA contract 1407. A.D.S. acknowledges CAPES – Brazil (contract BEX 1661/98-1) for financial support. O.C. dedicates this work to his new born son Mathieu and his wife Martine.

References

Aufdenberg, J. P., Hauschildt, P. H., & Baron, E. 2002, ApJ, 344, 570

Berio, P., Stee, Ph., Vakili, F., et al. 1999, A&A, 345, 203

Bjorkman, J. E., & Cassinelli, J. P. 1993, ApJ, 409, 429

Bjorkman, K. S., Nook, M. A., Nordsiek, K. H., et al. 1997, ApJ, 477, 926

Cashwell, E. D., & Everett, C. J. 1959, A practical manual on the Monte Carlo Method for random walk problems, (New York: Pergamon)

Castor, J. I., Abbott, D. C., & Klein, R. I. 1975, ApJ, 195, 157

Cassinelli, J. P., & Hoffman, N. M. 1975, MNRAS, 173, 789

Coté J., Waters, L. B. F. M., & Marlborough, J.M. 1996, A&A, 307, 184

Chesneau, O., Rousselet-Perraut, K., Vakili, F., et al. 2000, SPIE, 4006, 531

Chesneau, O., Roche, M., Boccaletti, A. et al. 2000, A&AS, 144, 523

Domiciano de Souza, Vakili, F., Jankov, S., et al. 2002, A&A, 393, 345

Elias, N. M. 2001, ApJ, 549, 647

Hanbury Brown, R., Davis, J., & Allen, L. R. 1974, MNRAS, 168, 93

Harmanec, P., Morand, F., Bonneau, D., et al. 1996, A&A, 312, 879

Harries, T. J., Howarth, I. D., & Evans, C. J. 2002, MNRAS, 337, 341

Herald, J. E., Hillier, D. J., & Schulte-Ladbeck, R. E. 2001, ApJ, 548, 932

Hillier, D.J., Crowther, P. A., Najarro, F., & Fullerton, A. W. 1998, A&A, 340, 483

Hoffman, J. L., Nordsieck, K. H., & Fox, G. K. 1998, AJ, 115, 1576

Jacob, A. P., & Scholz, M. 2002, MNRAS, 336, 1377

Kudritzki, R. P., Simon, K. P., & Hamann, W.-R. 1983, A&A, 118, 245

Lamers, H. J. G. L. M., Zickgraf, F.-J., de Winter, D., et al. 1998, A&A, 340, 117

Lamers, H. J. G. L. M., & Cassinelli, J.P. 1999, Stellar Winds (Cambridge Univ. Press)

Melgarejo, R., Magalhães, A. M., Carciofi, A. C., & Rodrigues, C. V. 2001, A&A, 377, 581

Mourard, D., Bonneau, D., Glentzlin, A., et al. 2000, SPIE, 4006, 434

Mourard, D., Clausse, J.-M., Pedretti, E., et al. 2000, SPIE, 4006, 541

Mourard, D., Abe, L., Domiciano, A., et al. 2003, SPIE, 4838, 9

Najarro, F. 2001, ASP Conf. Proc., 233, 133

Nordsieck, K. H., Wisniewski, J., & Babler, B. L. 2001, ASP Conf., 233, 261

Oudmaijer, R. D., & Drew J. E. 1999, MNRAS, 305, 166

Poeckert, R., & Marlborough, J.M., ApJ, 220, 940

Quirrenbach, A., Bjorkman, K. S., Bjorkman, J. E., et al. 1997, ApJ, 479, 477

Rodrigues, C.V., & Magalhães, A. M. 2000, ApJ, 540, 412

Rousselet-Perraut, K., Vakili, F., Mourard 1996, Opt. Eng., 35(10), 2943

Rousselet-Perraut, K., Vakili, F., Mourard, D., et al. 1997, A&AS, 123, 173

Rousselet-Perraut, K. 1998, A&AS, 131, 361

Rousselet-Perraut, K., Chesneau, O., Berio, Ph., & Vakili, F. 2000, A&A, 354, 595

Rousselet-Perraut, K., Chesneau, O., Vakili, F., et al. 2003, SPIE, 4843, 448

Sams, D. C., & Johnston, I. D. S. 1974, MNRAS, 168, 463

Stee, P., de Araùjo, F. X., Vakili, F., et al. 1995, A&A, 300, 219

Taylor, M., Nordsieck, K. H., Schulte-Ladbeck, R. E., & Bjorkman, K. S. 1991, AJ, 102, 1197

Vakili, F. 1981, A&A, 101, 352

Vakili, F., Mourard, D., Bonneau, D., Morand, F., & Stee, Ph. 1997, A&A, 323, 183

Vakili, F., Mourard, D., Stee, Ph., et al. 1998, A&A, 335, 261

Vakili, F., Chesneau, O., Delplancke, F., et al. 2001, Proc. ESO Workshop, Scientific Drivers for ESO Future VLT/VLTI Instrumentation, 331

Waters, L. B. F. M. 1986, A&A, 162, 121

Waters, L. B. F. M., & Marlborough, J. M. 1992, A&A, 256, 195

Wolf., S., Henning, Th., & Stecklum, B. 1999, A&A, 439, 839

Wolf, S., & Henning, Th. 2000, Comp. Phys. Comm., 132, 166

Wolf, S. 2003, Comp. Phys. Comm., 150, 99

Wood, K., Bjorkman, K. S., Whitney, A., Code, A. D. 1996, ApJ, 461, 828

Wood, K., Bjorkman, K. S., & Bjorkman, J. E. 1997, ApJ, 477, 926

Yudin, R. V., & Evans, A. 1998, A&AS, 131, 401

Zickgraf, F.-J., Wolf, B., Stahl, O., et al. 1985, A&A, 163, 119